Journal of Applied Mechanics Vol.9, pp.783-794 (August 2006) JSCE

2D Numerical model for river flow and bed evolution based on unstructured mesh

Hao ZHANG*, Hajime NAKAGAWA*, Yasunori MUTO*, Daizaburou TOUCHI** and Yoshio MURAMOTO***

*Member of JSCE, Disaster Prevention Research Institute, Kyoto University
**Student Member of JSCE, Graduate School of Engineering, Kyoto University
***Fellow of JSCE, Professor Emeritus of Kyoto University
(Shimomisu, Yoko-oji, Fushimi-ku, Kyoto 612-8235, Japan)

This paper describes a 2D (Two-dimensional) numerical model, through which the flow field and bed evolution in alluvial channels can be simulated. The model is formulated on an unstructured mesh using FVM (Finite volume method) and allows employment of hybrid polygons. This model calculates the velocity field by solving the unsteady shallow water equations with the widely used k-ε model for the turbulence closure. The bed evolution is simulated through the sediment continuity equation with an empirical formula for the bedload transport rate. The secondary flow effects on both the mean flow and the near-bed flow are considered. The model has been applied to predict the flow and bed evolution in a large-scale physical model experiment in a river restoration project. It is shown that the simulation result has a reasonable accuracy.

Key Words: *unstructured mesh, secondary flow, large-scale physical model, FVM*

1. Introduction

Numerical simulation of the flow and sediment process in alluvial rivers is one of the most challenging problems in the hydraulic engineering. On the one hand, the river flow is generally very complex due to the uneven bed topography, irregular banklines, changeable water surfaces and different kinds of hydraulic structures. On the other hand, the existing methods for sediment transport usually involve strong empiricism and introduce many uncertainties. There remains a lot of unknown on the mechanism of sediment transport despite the rapid development of the related research in recent years. Moreover, the flow and sediment process are strongly coupled and form a dynamic feedback system, together with the riverbed evolution.

In order to overcome or circumvent the inherent difficulties in the problem, many investigators have contributed to the seeking of more cost-effective solutions. Over the past several decades, unstructured mesh has exhibited its advantages in treating flows in complicated domains where it becomes impossible or intractable with structured mesh. Typical researches have been reported by Zhao et al. (1994) [1] who developed an unstructured 2D model for river basins based on the FVM formulation. In their model, they calculated the mass and momentum fluxes across the CV (Control volume) surfaces as a local 1D Riemann problem and solved this problem with an approximate Riemann solver. This idea has been followed and extended later by a lot of researchers such as Anastasiou and Chan (1997) [2], Sleigh et al. (1998) [3], Bradford and Sanders (2002) [4] and Yoon and Kang (2004) [5]. Kim et al. (1997) [6] presented an unstructured mesh based RANS (Reynolds-averaged Navier-Stokes) equations solver. The Rhie-Chow momentum interpolation method [7] was adopted for the calculation of surface fluxes. Mesh adaptation was also illustrated through computational examples. Recently, Nguyen et al. (2006) [8] introduced a solver for 2D Saint-Venant equations using the Rhie-Chow interpolation. The treatment of the source terms has been emphasized in their work.

According to reported computational tests, all of the preceding models were generally able to simulate selected experimental flows and/or river flows under fixed bed conditions. However, the extension from fixed bed to movable bed conditions has been rarely completed successfully with unstructured mesh methods. Amongst recent publications, the structured mesh based model is still predominant when sediment transport is involved. For example, the models proposed by Kassem and Chaudhry (2002) [9], Soulis (2002) [10],

Wu (2004) [11], Jang and Shimizu (2005) [12] as well as some well-known software packages such as the DELFT2D (WL | Delft Hydraulics), MIKE21 (Danish Hydraulic Institute) and CCHE2D (University of Mississippi). Most of them have employed boundary fitted structured mesh system to account for the complex geometries. Unfortunately, this kind of mesh makes the governing equations much more complex and does not allow local mesh refinement and mesh adaptation. Hence, there still exists inherent gap between the model formulation and practical use. In view of these arguments, a numerical model based on an unstructured mesh is probably the most attractive solution for the modeling of river flow and bed evolution.

In this paper, an attempt has been made to construct a practicable morphological model based on unstructured mesh. The flow field is obtained by solving the unsteady shallow water equations for open channels. Secondary flow affects both the mean flow field and the sediment transport. For the former, it is taken into account by adjusting a dimensionless diffusivity coefficient in the depth-averaged k-ε model as suggested by Minh Duc et al. (2004) [13]. And for the latter, the effect is expressed by estimating the near-bed flow field from the mean flow field. The bed evolution is simulated through the sediment continuity equation with the Ashida-Michiue formula [14] for the bedload transport rate. A bed slope factor is introduced to express the difference in the transport rate between on a sloping bed and on a horizontal bed. For a preliminary application, the model is applied to simulate the flow and bed evolution in a large-scale physical model experiment.

2. Flow model

2.1 Mean flow field

Integrating the 3D (Three-dimensional) RANS equations from the riverbed to the free surface, the following equations governing the 2D open channel flow can be derived.

$$\frac{\partial H}{\partial t}+\frac{\partial}{\partial x}(hu)+\frac{\partial}{\partial y}(hv)=0 \tag{1}$$

$$\frac{\partial u}{\partial t}+u\frac{\partial u}{\partial x}+v\frac{\partial u}{\partial y}=-g\frac{\partial H}{\partial x}+\frac{1}{\rho h}\left[\frac{\partial}{\partial x}(h\tau_{xx})+\frac{\partial}{\partial y}(h\tau_{xy})\right]-\frac{\tau_{bx}}{\rho h} \tag{2}$$

$$\frac{\partial v}{\partial t}+u\frac{\partial v}{\partial x}+v\frac{\partial v}{\partial y}=-g\frac{\partial H}{\partial y}+\frac{1}{\rho h}\left[\frac{\partial}{\partial x}(h\tau_{yx})+\frac{\partial}{\partial y}(h\tau_{yy})\right]-\frac{\tau_{by}}{\rho h} \tag{3}$$

where t= time; H = water stage (i.e. $H=h+z_b$); h = water depth; z_b = bed elevation; x, y= Cartesian coordinate components; u, v = depth-averaged flow velocity components in the x and y directions, respectively; g= gravitational acceleration; ρ = fluid density, τ_{xx}, τ_{xy}, τ_{yx}, τ_{yy} = depth-averaged turbulent stresses and τ_{bx}, τ_{by} = bottom shear stresses. Strictly speaking, the bottom shear stresses are related to the near-bed flow field rather than the mean flow field. Nevertheless, the commonly adopted quadratic friction law is used so far in the calculation of the mean flow velocity, which results in the following expressions:

$$\tau_{bx}=\rho c_f u\sqrt{u^2+v^2} \qquad \tau_{by}=\rho c_f v\sqrt{u^2+v^2} \tag{4}$$

in which the bottom friction coefficient c_f is related to the Manning's roughness coefficient n by

$$c_f=\frac{n^2 g}{h^{1/3}} \tag{5}$$

From Equation 4 and Equation 5, the near-bed shear velocity u_* is easily obtained. It is one of the most important factors for the near-bed sediment transport.

Approximating the turbulent stresses with Boussinesq's eddy viscosity concept, one has

$$\tau_{ij}=\rho\upsilon_t\left(\frac{\partial u_i}{\partial x_j}+\frac{\partial u_j}{\partial x_i}\right)-\frac{2}{3}k\rho\delta_{ij} \quad (i,j=x,y) \tag{6}$$

where υ_t = eddy viscosity, k = depth-averaged turbulence kinetic energy and δ_{ij}= Kronecker delta. In the zero-equation model, the eddy viscosity is usually estimated by

$$\upsilon_t=\frac{\kappa}{6}u_* h \tag{7}$$

where κ = van Karman constant (=0.41 in this study). In the k-ε model, the eddy viscosity is a function of the turbulent kinetic energy k and its dissipation rate ε, i.e.

$$\upsilon_t=c_\mu\frac{k^2}{\varepsilon} \tag{8}$$

where c_μ = coefficient and is usually set to be a constant 0.09. The two quantities k and ε are solved from their transport equations as follows, respectively.

$$\frac{\partial k}{\partial t}+u\frac{\partial k}{\partial x}+v\frac{\partial k}{\partial y}=\frac{\partial}{\partial x}\left(\frac{\upsilon_t}{\sigma_k}\frac{\partial k}{\partial x}\right)+\frac{\partial}{\partial y}\left(\frac{\upsilon_t}{\sigma_k}\frac{\partial k}{\partial y}\right)+P_h+P_{kv}-\varepsilon \tag{9}$$

$$\frac{\partial \varepsilon}{\partial t}+u\frac{\partial \varepsilon}{\partial x}+v\frac{\partial \varepsilon}{\partial y}=\frac{\partial}{\partial x}\left(\frac{\upsilon_t}{\sigma_\varepsilon}\frac{\partial \varepsilon}{\partial x}\right)+\frac{\partial}{\partial y}\left(\frac{\upsilon_t}{\sigma_\varepsilon}\frac{\partial \varepsilon}{\partial y}\right)+c_{1\varepsilon}\frac{\varepsilon}{k}P_h+P_{\varepsilon v}-c_{2\varepsilon}\frac{\varepsilon^2}{k} \tag{10}$$

where

$$P_h=\upsilon_t\left[2\left(\frac{\partial u}{\partial x}\right)^2+2\left(\frac{\partial v}{\partial y}\right)^2+\left(\frac{\partial u}{\partial y}+\frac{\partial v}{\partial x}\right)^2\right] \tag{11}$$

$$P_{kv}=\frac{u_*^3}{hc_f^{1/2}} \qquad P_{\varepsilon v}=\frac{c_{2\varepsilon}c_\mu^{1/2}}{(e_*\sigma_t)^{1/2}c_f^{3/4}}\frac{u_*^4}{h^2} \tag{12}$$

in which σ_t = Schmidt number expressing the relation between the eddy viscosity and the diffusivity for scalar transport (a value of 1.0 is adopted) and e_* = adjustable dimensionless diffusivity. The model constants generally take universal values as below[15].

$$\sigma_k=1.0 \quad \sigma_\varepsilon=1.3 \quad C_{1\varepsilon}=1.44 \quad C_{2\varepsilon}=1.92 \tag{13}$$

During the depth-averaging of the RANS equations, some so-called dispersion terms due to vertical non-uniformities of the mean flow have been omitted in Equation 2 and Equation 3 [15]. These terms exhibit similar physical effect with the turbulent stresses and can be significant when the secondary flow is obvious. Minh Duc et al. (2004) [13] suggested to adjust the dimensionless diffusivity to indirectly account for this effect according to their numerical experiments. A value of 0.15 has been suggested for laboratory flumes. In natural rivers, a value from 0.6 up to 10 might be used. Following their idea, the dimensionless diffusivity is treated as an adjustable parameter to include the effect of the secondary flow on the mean flow in this study. In practice, this parameter is firstly tuned by conducting fixed-bed computation. After that, the simulation of movable bed is started.

2.2 Near-bed flow field

Evaluation of the near-bed velocity is of significant meaning for the simulation of the sediment transport and bed evolution. It is generally accepted that the bed load transport driven by the bed shear is closely related to the near-bed velocity. Unfortunately, the direction and magnitude of the near-bed flow usually doe not coincide with those of the mean flow (i.e., the depth-averaged flow) in natural rivers, especially in meandering rivers.

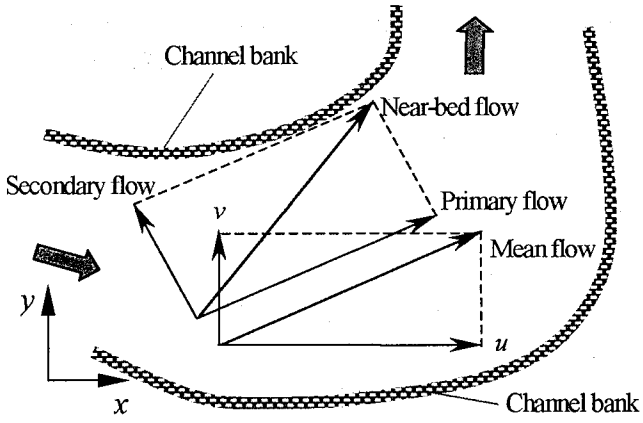

Fig. 1 Sketch of mean flow and near-bed flow directions

In order to estimate the near-bed flow field, the near-bed velocity is divided into a primary velocity U and a secondary flow velocity V (see Figure 1). The former has the same direction as that of the mean flow. The latter is normal to the primary velocity, and for simplicity, its magnitude can be estimated with Engelund's suggestion [16] for a fully developed bend flow. Hence,

$$U = a_U \sqrt{u^2 + v^2} \tag{14}$$

$$V = -\frac{h}{r} N_* U \tag{15}$$

where a_U = coefficient considering the primary velocity profile in the vertical direction (=1.0 in this study for simplicity); N_* = coefficient representing the intensity of the secondary flow (=7.0 for fully developed bend flows) and r = radius of curvature of the streamline. According to Shimizu and Itakura [17], it is estimated from the following equation

$$\frac{1}{r} = \frac{1}{\left(u^2+v^2\right)^{3/2}} \left[u\left(u\frac{\partial v}{\partial x} - v\frac{\partial u}{\partial x} \right) + v\left(u\frac{\partial v}{\partial y} - v\frac{\partial u}{\partial y} \right) \right] \tag{16}$$

3. Sediment transport

3.1 Governing equations

In the absence of suspended load, the bed variation is due to the movement of bed load transport in a thin layer near the riverbed. The sediment continuity equation in the bed load layer is expressed by

$$(1-\lambda)\frac{\partial z_b}{\partial t} + \left[\frac{\partial q_{bx}}{\partial x} + \frac{\partial q_{by}}{\partial y} \right] = 0 \tag{17}$$

where λ = porosity of sediment on the riverbed; q_{bx}, q_{by} = bed load transport rate in x and y direction, respectively. If the sediment transport rate is known, the bed deformation is immediately obtained.

Deterministic methods are generally used to evaluate the transport rate of bedload. With the Ashida-Michiue formula [14], one goes to the following expression

$$\frac{q_b}{\sqrt{(s-1)gd^3}} = 17\tau_{*e}^{3/2}\left(1-\sqrt{\frac{\tau_{*c}}{\tau_*}}\right)\left(1-\frac{\tau_{*c}}{\tau_*}\right) \tag{18}$$

where q_b= bed load discharge per unit width; s= specific gravity of sediment; g= gravitational acceleration; d= diameter of sediment; τ_{*e}, τ_{*c}, τ_* = dimensionless effective shear stress, critical shear stress and shear stress, respectively. The dimensionless shear stress is connected with the squared friction velocity u_*^2 and is defined as

$$\tau_* = \frac{u_*^2}{(s-1)gd} \tag{19}$$

Furthermore, the direction of the shear stress follows that of the near-bed velocity instead of the mean velocity as has been mentioned in the previous contexts.

3.2 Effect of local bed slope

Hydraulic structures such as bridge piers and groins have been widely constructed in rivers nowadays. This kind of structures function as local obstructions and will probably cause relatively steep local bed slope around them. In the simulation of the flow and bed evolution, the bed slope effect on the sediment transport is not negligible any more. Zhang et al. (2006) [18]

pointed out that the bed slope will affect the bed load transport in three ways: (a) the threshold condition, i.e. the condition just sufficient to initiate sediment motion; (b) the effective shear stress acting on the particle and (c) the direction of the sediment movement. Most of the existing literatures account for the bed slope effect under the presumption that the longitudinal flow is predominant. Nevertheless, the magnitudes of velocity components around local obstructions are usually comparable. Bearing this in mind, Zhang et al. (2006) suggested a way to consider the bed slope effect based on 3D force analyses of a particle on the bed. The basic idea is summarized here and details are referred to Zhang et al. (2006) and Zhang (2005) [19].

Similar to conventional treatments as concluded in van Rijn's publication [20], a bed slope factor is introduced to express the difference in the critical shear stress between on a sloping bed and on a horizontal bed. The bed slope factor is a function of the bed slope, angle of sediment repose as well as the near-bed flow velocity. It has been confirmed that conventional bed slope factors are special cases of the new bed slope factor if the longitudinal flow is predominant. The effective shear stress acting on the particle is a combined contribution from both the bottom shear stress and the particle gravity. The sediment transport direction coincides with that of the effective shear stress and is explicitly obtained in the analyses.

4. Boundary conditions

The boundaries in actual river conditions generally include the inlet, outlet and solid walls.

The hydrograph is usually known at the inlet boundary. The velocity is estimated according to the local conveyance, i.e.

$$u = K\frac{h^{2/3}}{n} \quad \text{where} \quad K = \frac{Q}{\Sigma \frac{h^{5/3}}{n} l} \tag{20}$$

in which Q = total discharge at a time step and l = length of the boundary. The turbulence kinetic energy is related to the velocity u and the turbulence intensity I as follow,

$$k = \frac{3}{2}ul^2 \tag{21}$$

The dissipation rate ε is estimated from Equation 8 by specifying a viscosity ratio (ν_t/ν) around 10-20.

At the outlet, water stage is known. Zero gradient boundaries are assumed for other quantities. Moreover, an ad hoc treatment is applied to correct the velocity components in order to assure the total mass conservation as follows

$$u = \frac{\Sigma Q_{in}}{\Sigma Q_{out}} u^{old} \qquad v = \frac{\Sigma Q_{in}}{\Sigma Q_{out}} v^{old} \tag{22}$$

where the discharges with subscripts *in* and *out* are the total discharges computed at inlet and outlet boundaries, respectively. The velocity component with a superscript *old* is the computed value with the numerical methods introduced in the next section.

At solid walls such as channel banks and emerged hydraulic structures, the standard wall function approach is used. However, the boundaries between wet and dry CVs (Control volumes) are not treated as solid walls. Since an implicit scheme has been used in the model, both wet and potential wet CVs participate in the calculation. Velocities and water depth are set to zero at the centers of the dry CVs. Special algorithms are proposed in this paper to account for the dry-wet boundaries.

5. Numerical scheme

5.1 Discretization methods

In a Cartesian coordinate system, the governing equations for the flow have a common form as below.

$$\frac{\partial}{\partial t}(h\phi) + \frac{\partial}{\partial x}(hu\phi) + \frac{\partial}{\partial y}(hv\phi) = \frac{\partial}{\partial x}\left(h\Gamma\frac{\partial \phi}{\partial x}\right) + \frac{\partial}{\partial y}\left(h\Gamma\frac{\partial \phi}{\partial y}\right) + s_\phi \tag{23}$$

where $h\Phi$ = transport quantity (for the momentum equations, such definitions are used for clarity: $M = hu$ and $N = hv$), Γ = diffusive coefficient and s_Φ = source term.

Equation 23 are integrated over CVs using the FVM on an unstructured mesh with a collocated variable arrangement and then submitted to discretization. The discretization adopts a term-by-term process. For the temporal term, the Euler scheme is employed. The power law scheme is used for the convection and diffusion terms. Surface fluxes are calculated following the idea of Rhie-Chow interpolation. Special techniques for unstructured meshes can be found in Nakagawa et al (2004) [21].

5.2 Velocity-pressure coupling

For the coupling of the velocity and pressure, the SIMPLER (Semi-implicit method for pressure-linked equation revised) procedure proposed by Patankar [22] is adopted. Considering the use of unstructured mesh, the procedure is summarized here.

After discretization, momentum equations for M and N at a CV surface have the form as

$$\begin{aligned} a_f M_f &= \Sigma a_{nb} M_{nb} - \int gh \frac{\partial H}{\partial x} dl\Big|_f + b_f \\ a_f N_f &= \Sigma a_{nb} N_{nb} - \int gh \frac{\partial H}{\partial y} dl\Big|_f + b_f \end{aligned} \tag{24}$$

where subscript f = the interface between two neighboring CVs; subscript nb = the neighboring CV; a = coefficient of the final discretized equations and b = source term excluding the pressure term. Defining pseudo-variables corresponding to M and N as

$$\hat{M}_f = \frac{\Sigma a_{nb} M_{nb} + b_f}{a_f} \qquad \hat{N}_f = \frac{\Sigma a_{nb} N_{nb} + b_f}{a_f} \tag{25}$$

Equation 24 can be written as

$$M_f = \hat{M}_f - \frac{\int gh \frac{\partial H}{\partial x} dl\big|_f}{a_f} \qquad N_f = \hat{N}_f - \frac{\int gh \frac{\partial H}{\partial y} dl\big|_f}{a_f} \quad (26)$$

In the derivation below, the guessed pressure and the velocity component resulted from the momentum equation not satisfying the continuity equation are denoted with an superscript *, the correction of an variable is denoted with an index ' and the variable without any superscript stands for the final value, i.e.

$$M = M^* + M' \qquad N = N^* + N' \qquad H = H^* + H' \quad (27)$$

With these definitions and Equation 24, it is readily to see

$$\begin{aligned} a_f M_f^* &= \Sigma a_{nb} M_{nb}^* - \int gh \frac{\partial H^*}{\partial x} dl\big|_f + b_f \\ a_f N_f^* &= \Sigma a_{nb} N_{nb}^* - \int gh \frac{\partial H^*}{\partial y} dl\big|_f + b_f \end{aligned} \quad (28)$$

Subtracting Equation 28 from Equation 24 and taking Equation 27 into account, one obtains the velocity correction

$$\begin{aligned} M_f' &= \frac{\Sigma a_{nb} M_{nb}'}{a_f} - \frac{\int gh \frac{\partial H'}{\partial x} dl\big|_f}{a_f} \\ N_f' &= \frac{\Sigma a_{nb} N_{nb}'}{a_f} - \frac{\int gh \frac{\partial H'}{\partial y} dl\big|_f}{a_f} \end{aligned} \quad (29)$$

If the first term on the right hand side is omitted, the velocity correction has a simple relationship with the pressure correction. Introducing this relationship into Equation 27, one goes to Equation 30.

$$M_f = M_f^* - \frac{\int gh \frac{\partial H'}{\partial x} dl\big|_f}{a_f} \qquad N_f = N_f^* - \frac{\int gh \frac{\partial H'}{\partial y} dl\big|_f}{a_f} \quad (30)$$

It is found that Equation 30 has almost the same form as Equation 26. In order to assure the mass conservation, the continuity equation for each CV should be satisfied, i.e.

$$\int \frac{\partial H}{\partial t}\big|_P + \Sigma \left(M_f l_x + N_f l_y \right) = 0 \quad (31)$$

where subscript P = the present approximated CV;

Substituting Equation 26 and Equation 30 into Equation 31, one has the so-called pressure equation and pressure-correction equation for H and H', respectively. The calculation sequences are therefore can be outlined as follows.

(1) Calculate the coefficients in the momentum equations. Omit the pressure term and solve for the pseudo-velocities.
(2) With the pseudo-velocities, the pressure equation is solved. This leads to the water stage and water depth.
(3) Based on the resulted water stage, solve the momentum equations to get the approximated velocity components.
(4) The resulted velocity components are used to calculate the mass fluxes through CV faces with the Rhie-Chow interpolation method. Solve the pressure-correction equation to obtain the pressure correction.
(5) From the pressure correction, the velocity correction is obtained. And correct the velocity field.
(6) Solve the transport equations for the turbulence kinetic energy and its dissipation rate, respectively. And then update the eddy viscosity.
(7) Repeat the above procedures until the residual level becomes sufficiently small or the prescribed maximum iteration step number is covered.

At the dry-wet boundary, the surface fluxes are not properly estimated with any linear interpolation method due to the steep gradient of the pressure. Furthermore, the zero velocity and water depth at the center of the dry CV bring numerical problems when calculating the velocity correction by using the pressure correction. Hence some ad hoc treatments are needed between step (4) and step (5) to account for the dry-wet boundary.

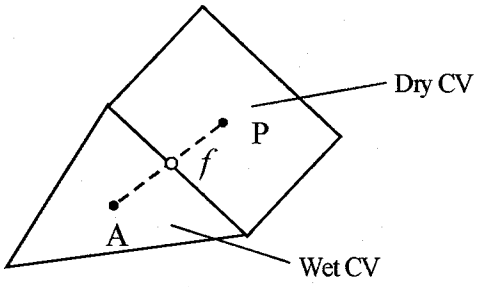

Fig. 2 Treatment of the dry-wet boundary

The pressure correction in Step (4) is firstly used to correct surface fluxes (denoted with subscript *new*) around dry CVs, i.e.

$$M_{f,new}^* = M_f^* - \frac{ghl_x}{a_f}\left(H_A' - H_P'\right) \qquad N_{f,new}^* = N_f^* - \frac{ghl_y}{a_f}\left(H_A' - H_P'\right) \quad (32)$$

where subscript A = the adjacent CV (i.e. wet CV) and l_x, l_y = projected length of the dry-wet boundary. The new fluxes are then introduced into Equation 30. Considering Equation 31 for mass conservation, a new pressure correction for the dry CV is

$$H_P' = \frac{ghH_A' \Sigma \frac{l^2}{a_f} - \Sigma \left(M_{f,new}^* l_x + N_{f,new}^* l_y \right)}{ghH_A' \Sigma \frac{l^2}{a_f} + A_P / \Delta t} \quad (33)$$

where A_p = area of present CV (i.e. dry CV) and Δt = time step.

Since the dry CV has a zero water depth in the previous time step, the pressure correction gives the new water stage directly. Other quantities such as a_p at the center of the dry CV can be estimated by linear interpolation from the surface values. Hence the dry CV can be treated as a common CV. Then program goes to step (5) with the updated pressure correction. This treatment is found to provide an effective way to account for the water edges shifting without significant increasing of computational cost.

6. Model application

The numerical model is applied to simulate the flow field and bed evolution in a large-scale physical model experiment corresponding to a river restoration project. The study area of the project covers a 3km-long stretch of the Kizu River in west Japan. The Kizu River transports a great amount of sediment and is famous for its unique river scenery. It locates in the Yodo River basin which ranks No. 7 amongst Japan's main rivers in terms of catchment area [23]. Figure3 shows the detailed location of the study domain. In the stretch considered, there is an ancient wooden bridge: Nagare Bridge. Around this bridge there forms a representative sightseeing and recreation spot. Unfortunately, a typhoon-induced flood in August 2004 brought great damage to this area. Groins have been built and are still planned to build around the bridge for the maintenance and recovery of the river scenery (see Figure 4). The main objectives of this project are to understand the underlying processes and mechanisms of the flow and bed evolution due to groin constructions and seek the most cost-effective solution to restore the natural scenery unique to the river with experimental and numerical methods.

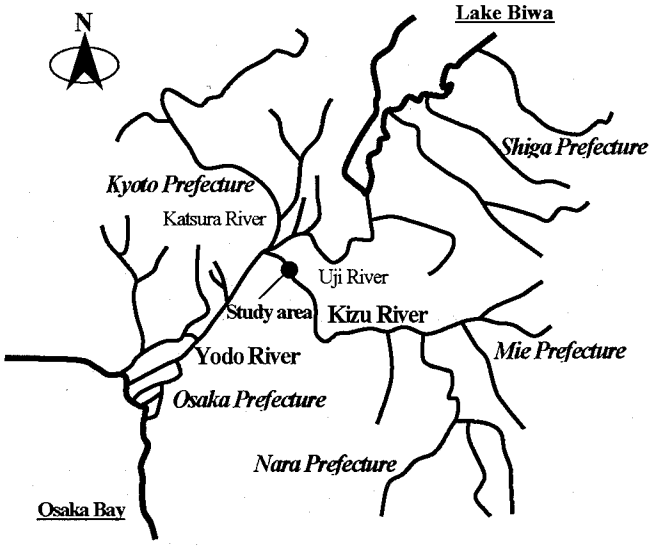

Fig. 3 Location of study area

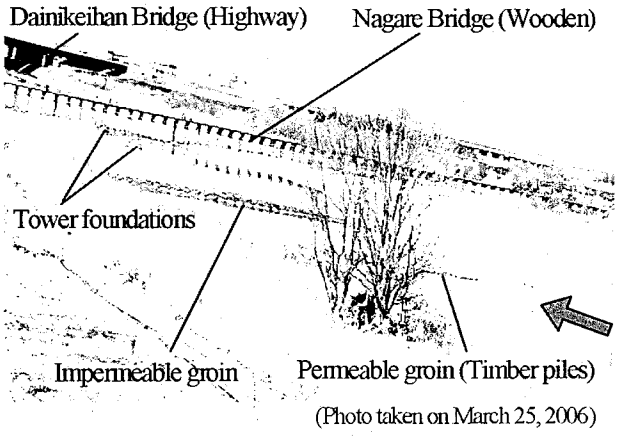

Fig. 4 Location of local hydraulic structures (bridges and groins)

The physical model was constructed in the Ujigawa Hydraulics Laboratory, Kyoto University, Japan. The model represented the river section from 4.4km to 7.4km with a physical scale of 1:65. Along the transverse section, the river typically consisted of a low flow channel with floodplains on both sides. The floodplain was treated as fixed bed, while the low flow channel was movable and covered with model sediment. Hydraulic structures such as the piers of the Dainikeihan Bridge, support of the Nagare Bridge (a series of timber piles), impermeable and permeable (group of timber piles) groins were represented to scale in the experiment. The model sediment has been selected as coal powder with a mean diameter of 0.83mm and a specific gravity of 1.41. Continuous sediment supply was guaranteed during the experiment through an automatic sediment supplier installed at the inlet boundary. At the outlet boundary, a tailgate was used to control the water stage. A point gauge set at section 4.6km was employed to record the downstream water depth. Field data of some control sections surveyed in February 2005 was used to shape the initial bed configuration. So far, several preliminary experiments have been carried out with different flow discharges and sediment inputs. For each experiment, the bed deformation and water level were measured at some intermediate stages. The former was measured with a sand-surface profiler and the latter with an ultrasonic sensor. Surface flow visualization with PIV (Particle image velocimetry) was conducted at the final equilibrium stage. After that, the bed was shaped back to the initial condition for a new experiment. The experimental setup is shown in Figure 5 and detailed information is referred to Touchi (2006) [24].

6.1 Description of the computational conditions

The computation is based on the model scale, but the result has been transformed to the prototype scale for clarity. The computational domain covers the same area as that represented by the physical model. Two kinds of flood conditions are investigated corresponding to water discharges of 500m^3/s and 2000m^3/s, respectively. Both fixed bed and movable bed calculations have been carried out as summarized in Table 1.

Table 1 Computational cases

Case	Discharge	Bed condition
1	500 m^3/s	Measured equilibrium bed (fixed bed)
2	2000 m^3/s	Measured equilibrium bed (fixed bed)
3	2000 m^3/s	Bed from initial to 160h (movable bed)

For the fixed bed calculation, the bed level for each CV is interpolated from the measured data at equilibrium stage (Case 1 at 564h and Case2 at 272h) in the experiments. In the case of the movable bed calculation (Case 3), the initial bed elevation is interpolated from field data of control sections. The longitudinal distance between two consecutive sections is about 50m.

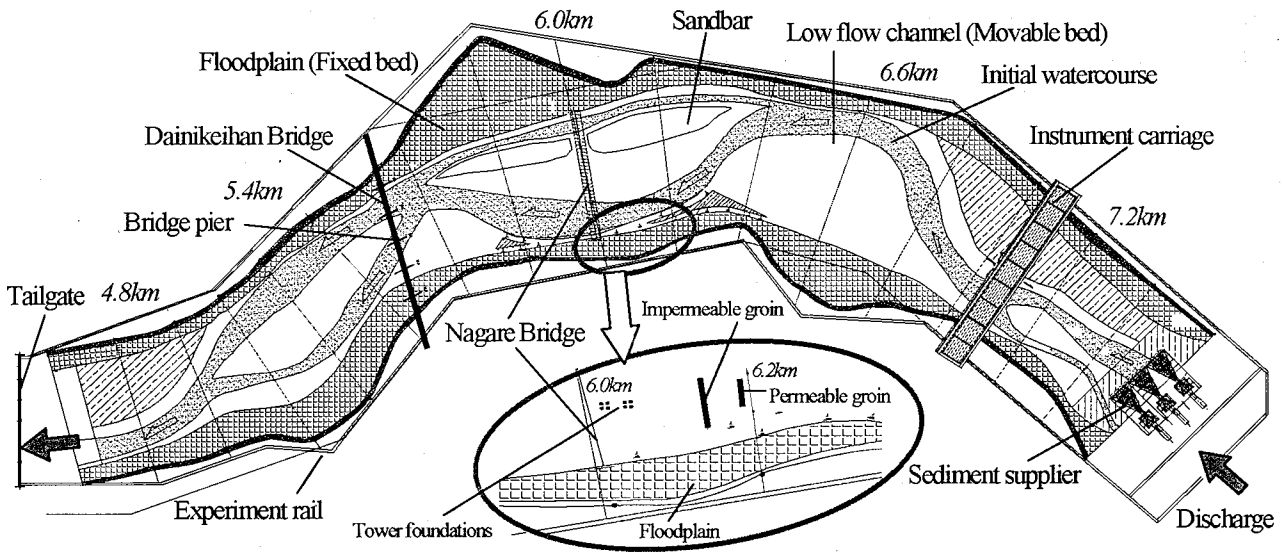

Fig. 5 Setup of the physical model experiment and sketch of the initial planform

The same mesh system, showing in Figure 6, is used for all computational cases. The total number of CVs employed is 14,531. The details (e.g. shape, number and layout) of the timber piles supporting the Nagare Bridge and consisting the permeable groin are not accurately resolved from the perspective of computational convenience. The CVs containing the piles are considered as roughness elements in the calculation. The Manning's roughness coefficient n is assigned a slightly larger value to these CVs.

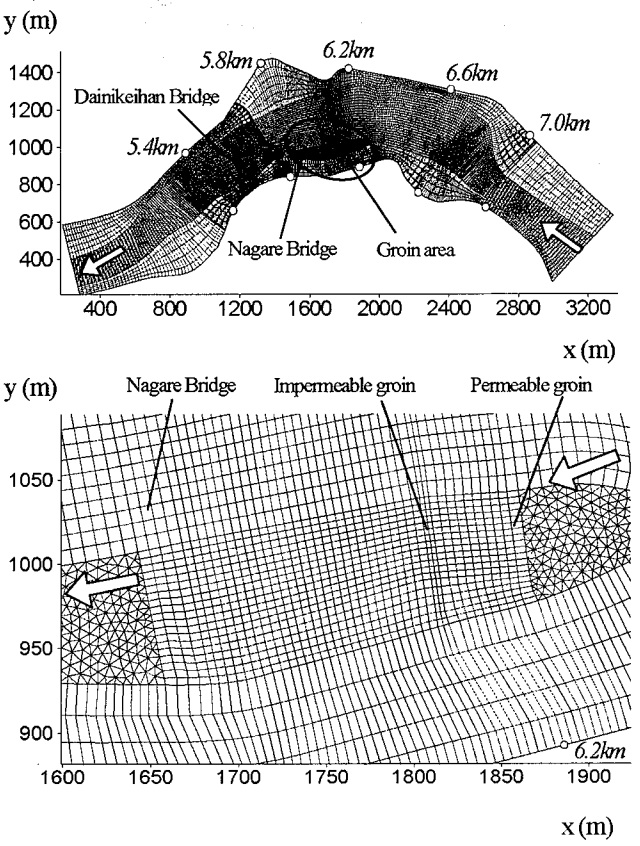

Fig. 6 Mesh system (General view: Top; Groin area: Bottom)

Both quadrilaterals and triangles have been used in the calculation. Hence the complex geometries can be accurately resolved. In the low flow channel, the mesh is fine. The finest mesh is generated around the groins and the Nagare Bridge, which allows a highest distance resolution of about 2.5m.

For each case, the zero-equation model is firstly applied to calculate the turbulent flow with any given velocity field (i.e. cold start). The result then serves as initial conditions for the final computation with the k-ε model.

6.2 Numerical result and discussion

(1) Velocity field

The mean flow velocity vectors (u, v) in the groin stretch are shown in Figure 7 (Case 1) and Figure 11 (Case 2). For the time being, the measured mean velocity is not available. Therefore, the surface flow visualization and PIV results are presented for reference. Considering the large width-depth ratio of the river flow, comparison and analysis of the flow pattern in these figures are of practical meaning.

The similarities between the computed mean flow and the observed surface flow are evident if one takes a look from Figure 7 to Figure 9 and Figure 10 to Figure 12, respectively.

However, the flow pattern changes significantly from Case 1 to Case 2, in particular the area around the sandbar in front of the groins (as sketched in Figure 5). In both cases, the sandbar area in front of the groins is submerged. The flow over the sandbar goes to the left side of the channel in case of small flood (Case 1) before it approaches the Nagare Bridge. While in larger flood case (Case 2), the flow over the sandbar gains a very large transverse velocity towards the right side of the channel. This is mainly attributed to different bed topographies and water stages due to different flood discharges. Small flood does not

significantly change the location of the sandbar. The watercourse along either side of the floodplain almost maintains. But in case of large flood, the sandbar shifts downstream and the wavelength of which also turns larger. The previous watercourse on the left side of the channel almost disappears. At the same time, bed elevation decreases very much in the groin area. Great pressure gradient between the sandbar area and the groin area hence causes obvious transverse velocity.

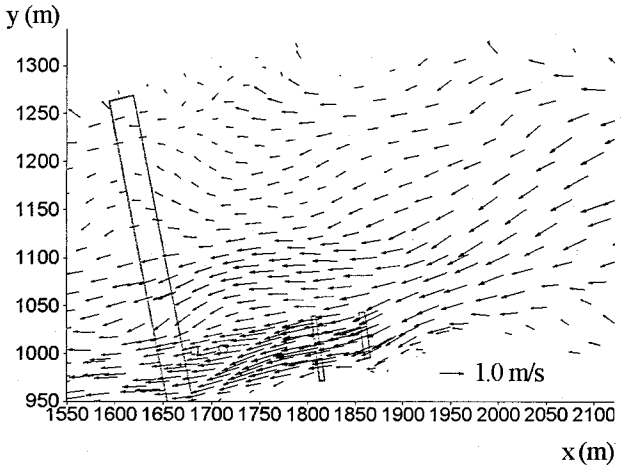

Fig. 7 Mean velocity in the groin stretch (Case1, Simulation)

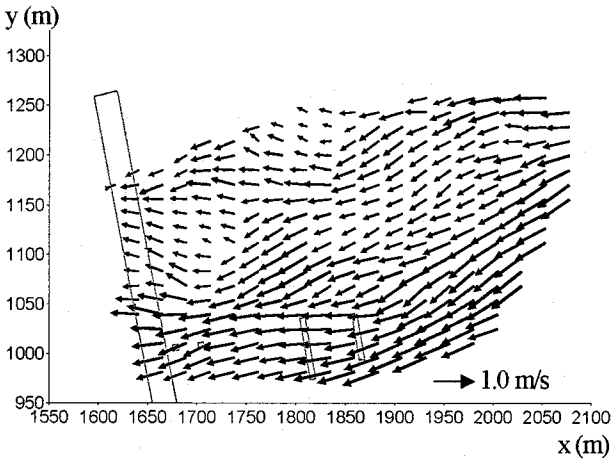

Fig. 8 Surface flow velocity in the groin stretch (Case1, PIV)

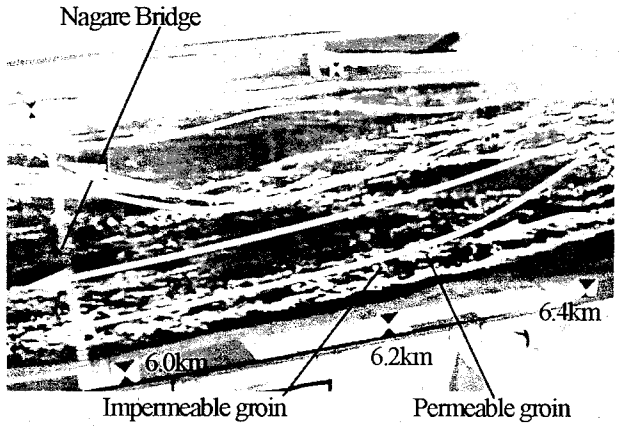

Fig. 9 Surface flow in the groin stretch (Case 1, Experiment)

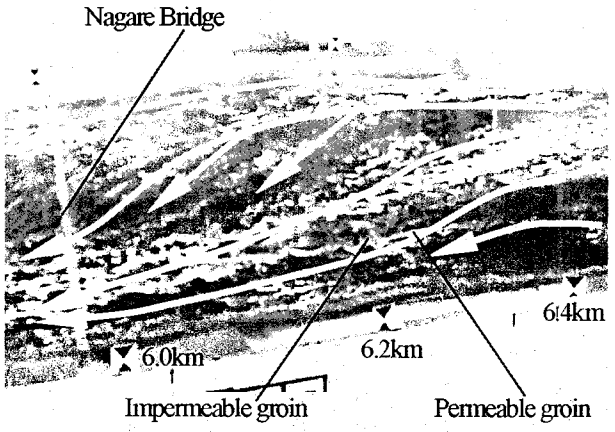

Fig. 10 Surface flow in the groin stretch (Case 2, Experiment)

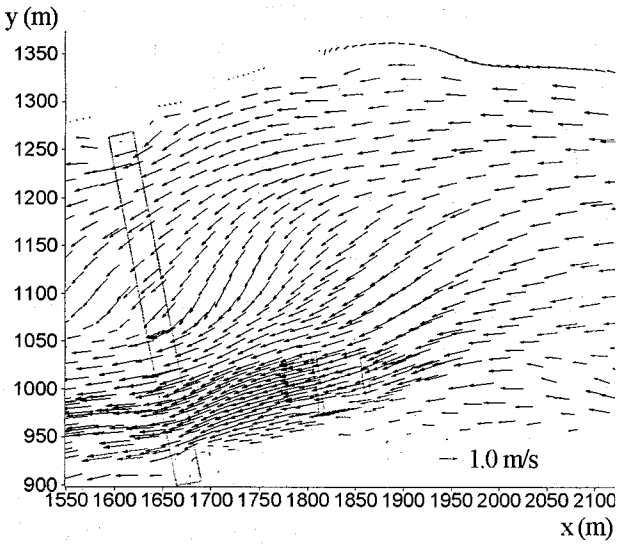

Fig. 11 Mean velocity in the groin stretch (Case 2, Simulation)

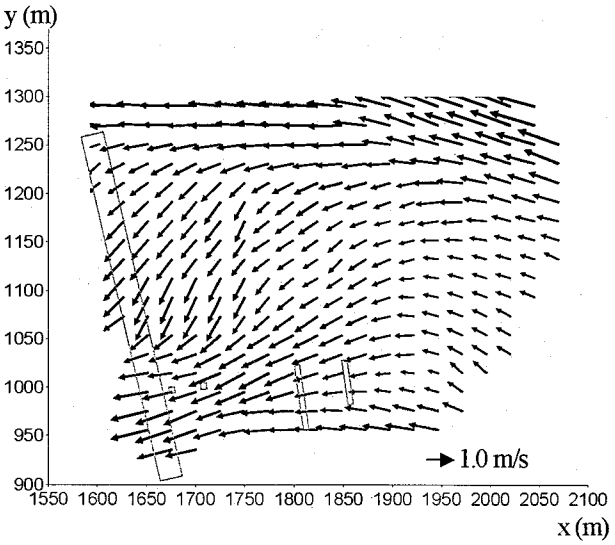

Fig. 12 Surface flow velocity in the groin stretch (Case 2, PIV)

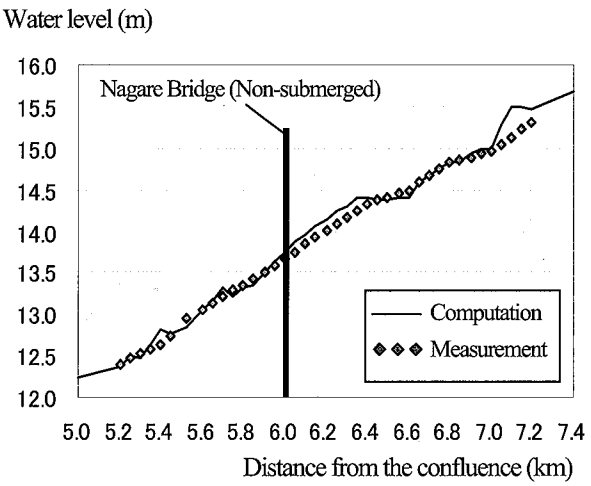

Fig. 13 Water level at center of low flow channel (Case1)

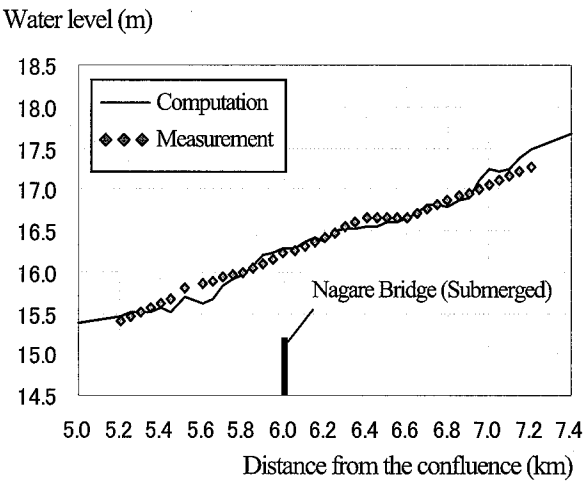

Fig. 14 Water level at center of low flow channel (Case 2)

(2) Water stage

The computed water level along the centerline of the low flow channel is compared with the experimental result as shown in Figure13 and Figure14. In both cases, the impermeable and permeable groins are submerged, while the Nagare Bridge is emerged in Case 1 but submerged in Case 2.

It is found that the prediction of the water level is quite well in both cases. Slightly over-estimation is observed in the most upstream sections. It is probably caused by the inlet boundary effect in both the numerical simulation and the physical model experiments. Generally speaking, the applicability of the proposed flow model can be confirmed.

(3) Bed evolution

The bed evolution under a 160-hour flood process with constant water discharge and sediment supply is investigated (i.e. Case 3). The discharge is 2000m^3/s and corresponds to the maximum annual discharge of the river.

Figure 15 shows the initial bed contour. Figure 16 is the simulated bed contour after continuous water discharge and sediment supply for 40 hours. Figure 17 and Figure 18 are the measured and computed bed contours after 80 hours, respectively. In Figure 19 and Figure 20, the bed contours after 160 hours are shown for the experiment and simulation correspondingly.

For the time being, measured data is only available at several representative transverse sections. The longitudinal distance between two consecutive sections is around 50m as has been mentioned before. It is much larger than the size of the groins. Hence the details of the local bed deformation around the groins are not accurately resolved from the experimental data so far. Considering this, more emphasis is put upon the general deposition-erosion pattern in the analyses hereafter.

Despite some differences in the values of the depositional and eroded depth in some area, the simulated deposition-erosion pattern (i.e. the pool-riffle morphology) exhibits much similarity with that of the experiment if one takes a look from Figure 17 to Figure 20.

The longitudinal movement of the two sandbars sketched in Figure 15 deserves special attention (denoted as Sandbar1 and Sandbar2, respectively). They are of crucial importance for the flow pattern and bed evolution in the interest area. It is evident that both sandbars gradually expand towards downstream with time. After 80 hours, the downstream part of Sandbar1 almost connects Sandbar2, and Sandbar2 extends to the piers of the Dainikeihan Bridge. The height of the sandbars also shows a tendency of increasing. It is in particular obvious according to the result of the experimental measurement.

The change of the sandbars has a significant effect on the location of the main stream. In the groin stretch, the initial watercourse on the left side is significantly deepened, while the one on the right side is almost colonized by Sandbar2. Along the transverse direction, the main stream crossing the Dainikeihan Bridge gradually shifts from the right side to the left side.

There are many factors that might be responsible for the differences between the computational and experimental results since the bed evolution process is a complex and dynamic feedback process. The error introduced in the flow model may strongly interact with that in the sediment transport model. As a result, these errors will either cancel out or augment with time. Right now, it is quite difficult to separate the error sources from one another. However, the comparison of the simulation result and experiment data still provides useful information for further improvements. For example, the effect of the secondary flow on the sediment transport rate seems under-estimated and the dimensionless diffusivity should be tuned with more data. The roughness of the CVs containing the Nagare Bridge appears a little large. It should be carefully selected after more calibrations.

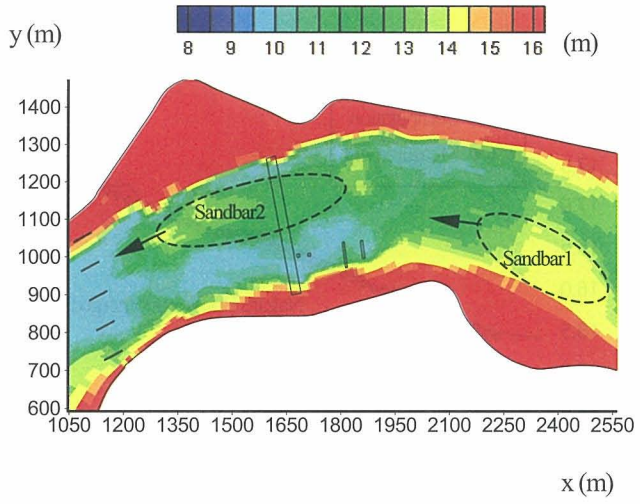

Fig. 15 Initial bed contour (Case 3, Experiment and Simulation)

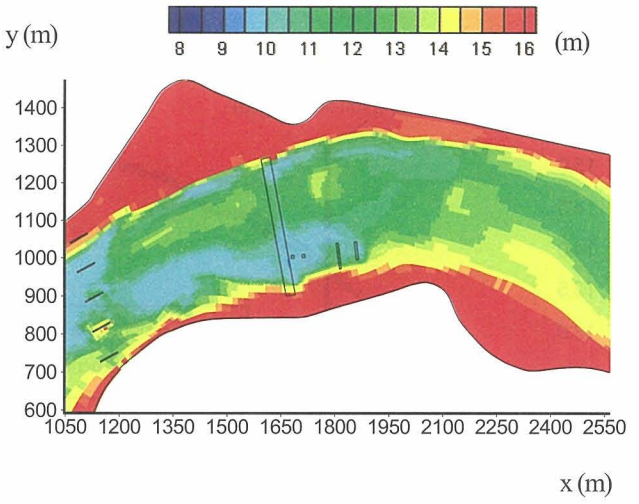

Fig. 16 Bed contour after 40 hours (Case 3, Simulation)

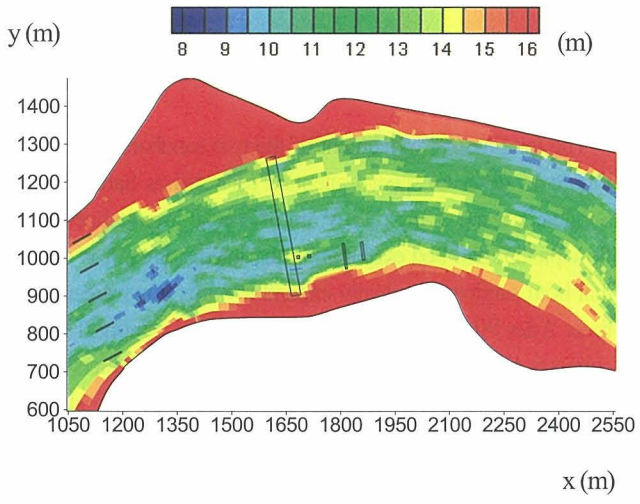

Fig. 17 Bed contour after 80 hours (Case 3, Experiment)

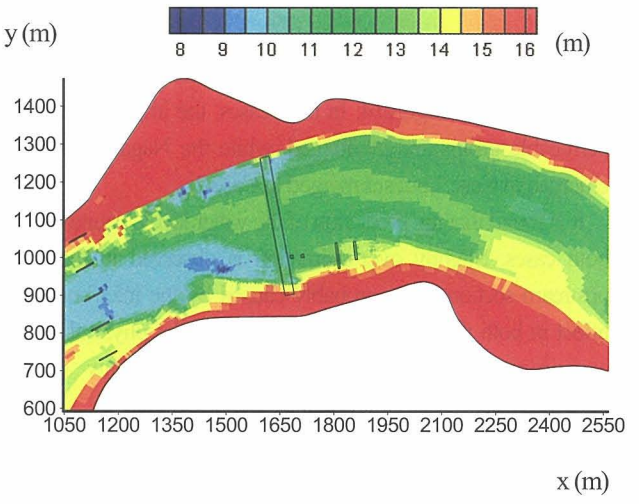

Fig. 18 Bed contour after 80 hours (Case 3, Simulation)

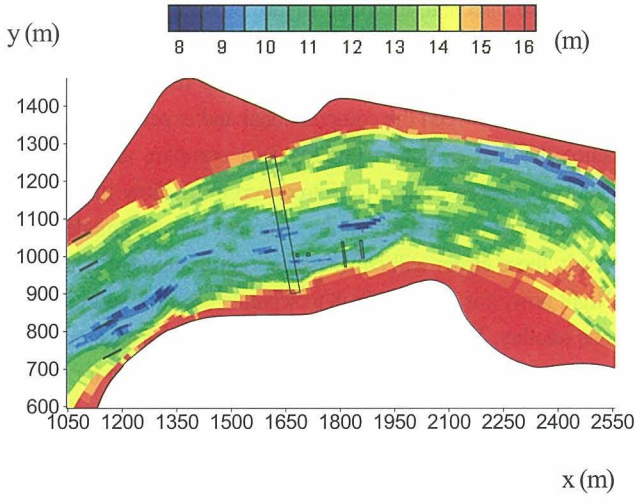

Fig. 19 Bed contour after 160 hours (Case 3, Experiment)

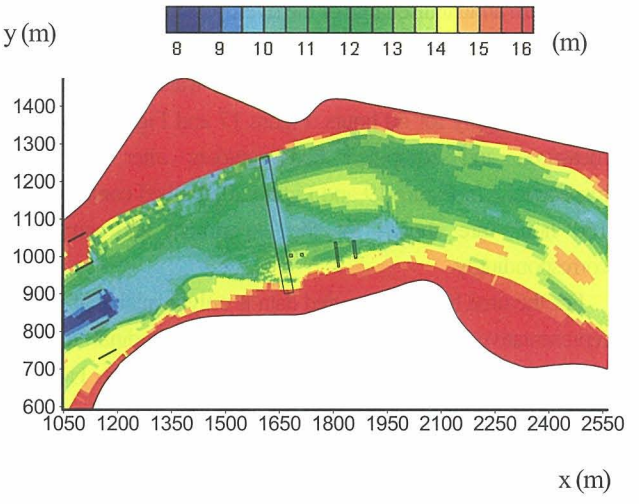

Fig. 20 Bed contour after 160 hours (Case 3, Simulation)

7. Conclusions

A morphological model has been presented and applied to predict the flow and bed evolution in a large-scale physical model experiment. Comparisons between the numerical simulation and the experimental measurement give quite encouraging result and demonstrate the applicability of the proposed model.

From a perspective of cost-effectiveness and practicability, the model simulates the flow field with the depth-averaged k- ε turbulence model and takes into account secondary flow effects on both the mean flow and the near-bed flow. The latter one is directly related to the near-bed shear stress and plays a crucial role in the bedload transport. Influence of the local bed slope on the sediment transport has been considered as well. The bed evolution is obtained by solving the sediment continuity equation in the bedload layer. Moreover, special treatment has been put forward to account for the dry-wet boundaries due to the change of bed configurations and shifting of water edges. Compared with most existing models in the literature (a brief overview may be found in Zhang, 2005 and Zhang et al., 2005[25]), the current model is formulated using the well-accepted FVM in CFD (Computational fluid dynamics) community based on an unstructured mesh system. This will probably achieve the best solution to accommodate special requirements in engineering practices such as the conservativeness of quantities, complex boundary resolution, mesh adaptation and so on.

It has to be pointed out that both the numerical model and the physical model experiment are still of preliminary and qualitative nature at the current stage. Inter-comparisons between the numerical model and the physical model results are expected to provide meaningful information on the flow and bed evolution in rivers with hydraulic structures. This information can be also of valuable reference for the further improvement of the numerical model and design optimization of the experiment to be conducted. Nevertheless, more calibrations and verifications are needed for the numerical model in order to get more confidence in the model performance. Measurements on the detailed information of the flow and bed deformation around the groin area are also necessary in the physical model experiment and have been planned to conduct in the near future.

Acknowledgement

Dr. Yasuyuki Baba (Kyoto University), Mr. Akira Nakanishi (Foundation of River & Watershed Environment Management), Mr. Michinari Tani and Mr. Hirokazu Ikeda (Japan Industrial Testing Corporation) are sincerely acknowledged.

REFERENCES

1) Zhao, D. H., Shen, H.W., Tabios, G.Q., Lai, J.S. and Tan, W. Y., Finite-volume two-dimensional unsteady-flow model for river basins, Journal of Hydraulic Engineering, ASCE, Vol. 120, No.7, 1994, pp.863-883
2) Anastasiou, K. and Chan, C. T., Solution of the 2D shallow water equations using the finite volume method on unstructured triangular meshes, International Journal for Numerical Methods in Fluids, Vol. 24, 1997, pp. 1225-1245
3) Sleigh, P.A., Gaskell, P.H., Berzins, M. and Wright, N.G., An unstructured finite volume algorithm for predicting flow in rivers and estuaries, Computers & Fluids, Vol. 27, No.4, 1998, pp. 479-508
4) Bradford, S. F. and Sanders, B. F., Finite-volume model for shallow-water flooding of arbitrary topography, Journal of Hydraulic Engineering, ASCE, Vol.128, No.3, 2002, pp.289-298
5) Yoon, T.H. and Kang, S.K., Finite volume model for two-dimensional shallow water flows on unstructured grids, Journal of Hydraulic Engineering, ASCE, Vol. 130, No. 7, 2004, pp. 678-688
6) Kim, S.E., Mathur, S.R., Murthy, J.Y. and Choudhury, D., A Reynolds-averaged Navier-Stokes solver using an unstructured mesh based finite-volume scheme, Fluent Technical Notes, (TN117), Fluent, Inc., 1997
7) Rhie, C.M. and Chow, W.L., Numerical study of the turbulent flow past an airfoil with trailing edge separation, Journal of AIAA, Vol. 21, 1983, pp. 1525-1532
8) Nguyen, D.K., Shi, Y.E., Wang, S.S.Y. and Nguyen, T.H., 2D shallow-water model using unstructured finite-volumes methods, Journal of Hydraulic Engineering, ASCE, Vol.132, No.3, 2006, pp.258-269
9) Kassem, A.A. and Chaudhry, M.H., Numerical modeling of bed evolution in channel bends, Journal of Hydraulic Engineering, ASCE, Vol. 128, No. 5, 2002, pp. 507-514
10) Soulis, J.V., A fully coupled numerical technique for 2D bed morphology calculations, International Journal for Numerical Methods in Fluids, Vol. 38, 2002, pp. 71-98
11) Wu, W., Depth-averaged two-dimensional numerical modeling of unsteady flow and nonuniform sediment transport in open channels, Journal of Hydraulic Engineering, ASCE, Vol.130, No.10, 2004, pp.1013-1024
12) Jang, C.L. and Shimizu, Y., Numerical simulations of the behavior of alternate bars with different bank strengths, Journal of Hydraulic Research, IAHR, Vol. 43, No. 6, 2005, pp. 596-612
13) Minh Duc, B., Wenka, T. and Rodi, W., Numerical modeling of bed deformation in laboratory channels, Journal of Hydraulic Engineering, ASCE, Vol.130, No.9, 2004, pp.894-904
14) Ashida, K. and Michiue, M.: Studies on bed load

transportation for nonuniform sediment and river bed variation. Disaster Prevention Research Institute Annuals, Kyoto Univ., No.14B, 1972, pp.259-273 (in Japanese)
15) Rodi, W., Turbulence Models and Their Application in Hydraulics - a State of the Art Review, University of Karlsruhe, Karlsruhe, Germany, 1980
16) Engelund, F., Flow and bed topography in channel bends, Journal of the Hydraulics Division, ASCE, Vol. 100, No. HY11, 1974, pp. 1631-1648
17) Shimizu, Y. and Itakura, T., Calculation of flow and bed deformation with a general non-orthogonal coordinate system, Proc. 24 IAHR Congress, Madrid, C-2, 1991, pp. 241-248.
18) Zhang, H., Nakagawa, Muto, Y., Baba, Y. and Ishigaki, T., Numerical simulation of flow and local scour around hydraulic structures, International Conference on Fluvial Hydraulics (RiverFlow2006), Lisbon, Portugal, Sept. 6-8, 2006 (accepted)
19) Zhang, H., Study on Flow and Bed Evolution in Channels with Spur Dykes, Doctoral Dissertation, Kyoto University, Kyoto, Japan, 2005
20) van Rijn, L.C., Principles of Sediment Transport in Rivers, Estuaries and Coastal Seas, AQUA Publications, Amsterdam, The Netherlands, 1993
21) Nakagawa, H., Zhang, H. Ishigaki, T. and Muto, Y., Prediction of 3D flow field with non-linear k-ε model based on unstructured mesh, Journal of Applied Mechanics, JSCE, Vol.7, 2004, pp.1077-1088
22) Patankar, S.V., Numerical Heat Transfer and Fluid Flow, McGraw-Hill, New York, 1980
23) Kinki Regional Development Bureau, Ministry of Land, Infrastructure and Transport, Japan, Lake Biwa and the Yodo River, 2002
24) Touchi, D., Investigation of Bed Evolution around Spur Dykes with Large Scale Physical Model Experiments, Bachelor's Thesis, Kyoto University, Kyoto, Japan, 2006 (in Japanese)
25) Zhang, H., Nakagawa, H., Ishigaki, T., Muto, Y. and Baba, Y., Three-dimensional mathematical modeling of local scour, Journal of Applied Mechanics, JSCE, Vol.8, 2005, pp. 803-812

(Received: April 13, 2006)